XENON SPUTTER YIELD MEASUREMENTS FOR ION THRUSTER MATERIALS *

John D. Williams, Michael M. Gardner, Mark L. Johnson, and Paul J. Wilbur
Department of Mechanical Engineering
Colorado State University
Fort Collins, CO 80523
Phone: (970) 491-8564
FAX: (970) 491-8671
e-mail: johnw@engr.colostate.edu

ABSTRACT

In this paper, we describe a technique that was used to measure total and differential sputter yields of materials important to high specific impulse ion thrusters. The heart of the technique is a quartz crystal monitor that is swept at constant radial distance from a small target region where a high current density xenon ion beam is aimed. Differential sputtering yields were generally measured over a full 180° arc in a plane that included the beam centerline and the normal vector to the target surface. Sputter yield results are presented for a xenon ion energy range from 0.5 to 10 keV and an angle of incidence range from 0º to 70° from the target surface normal direction for targets consisting of molybdenum, titanium, solid (Poco) graphite, and flexible graphite (grafoil). Total sputter yields are calculated using a simple integration procedure and comparisons are made to sputter yields obtained from the literature. In general, the agreement between the available data is good. As expected for heavy xenon ions, the differential and total sputter yields are found to be strong functions of angle of incidence. Significant under- and over-cosine behavior is observed at low- and high-ion energies, respectively. In addition, strong differences in differential yield behavior are observed between low-Z targets (C and Ti) and high-Z targets (Mo). Curve fits to the differential sputter yield data are provided. They should prove useful to analysts interested in predicting the erosion profiles of ion thruster components and determining where the erosion products re-deposit.

INTRODUCTION

As the interest in ion thrusters operated at high specific impulse builds, it is becoming increasingly important for analysts to have sputter yield data for a wide range of incident ion angles and energies.[1,2] Both total sputter yield (atoms/ion) and differential sputter yield (atoms/ion/steradian) are needed. These data are of interest for calculating erosion of spacecraft surfaces and thruster components that can be struck by high-energy ions produced in the beams of these thrusters.[3,4] Of equal interest is sputtering caused by ions with lower energies that are created via charge exchange reactions near ion thruster grid surfaces[1] or by potential hill structures located within ion thruster discharge chambers.[5,6] Sputter erosion of surfaces at cathode potential that face the interior of discharge chambers can also occur via bombardment from multi-charged ions produced within the discharge plasma.[7] These multi-charged ions can obtain energies corresponding to multiples of the anode to cathode potential difference, which can be well above the sputtering threshold[8] for most materials.

One important use of differential sputter yield data is in numerical simulations that are needed to calculate erosion profiles of accelerator grid surfaces and subsequent contamination buildup on adjacent grid surfaces, thruster components, and spacecraft surfaces. Detailed knowledge of the evolution of the eroded accelerator grid surface would allow thruster performance to be predicted over long mission times. Furthermore, sputter yield data are also needed to describe back sputter rates onto thruster and vacuum chamber surfaces from beam dumps in facilities where life tests and acceptance tests are performed. These data are needed to determine if the test facility is affecting the test results. In response to these needs, we have initiated an experimental and numerical program to provide sputter data corresponding to conditions unique to high specific impulse thrusters.

---

* Presented as paper IEPC-03-130 at the 28th Int'l Electric Propulsion Conf., Toulouse, France, 17-21 March 2003.
Copyright © 2003 by the Electric Rocket Propulsion Society. All rights reserved.

In this paper, we first present a description of our measurement technique, which consisted of a quartz crystal monitor that was swept at constant radial distance from a small target region where a high current density xenon ion beam was aimed. This section is followed by a presentation of data that has been collected to date. In addition to experimental data, curve fit coefficients are listed in tabular form to simplify the use of the measurements in models of electric propulsion devices.

SPUTTER YIELD MEASUREMENT TECHNIQUE

Sputter yield testing was performed by first clamping a planar target to a water-cooled mounting plate in a vacuum system, evacuating, and then baking the system. No-flow pressures below $1x10^{-6}$ Torr were achieved before testing was started. The basic test apparatus, which is shown schematically in Fig. 1, includes an ion source equipped with a well-focused, 2.5-cm diameter ion optics system. The ion beam is directed onto the center of the target surface, which is located 23 cm downstream of the ion source grids. This target surface, which is large compared to the beam size, can be rotated to change the angle of incidence of the beam (β). For this study, incidence angles were varied from β=0° to β=70°.

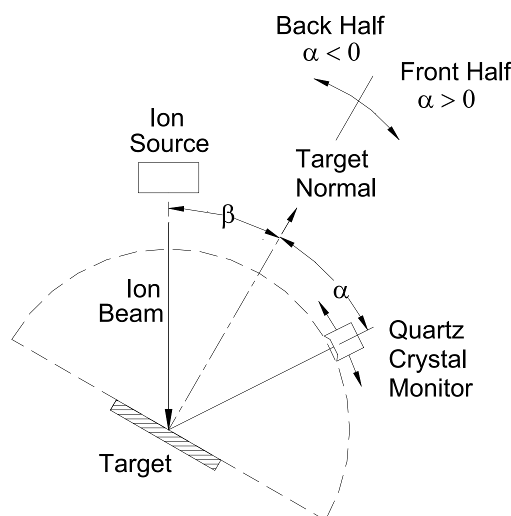

Fig. 1 Sketch of Test Apparatus.

Sputtered material was sensed as a mass accumulation rate by the quartz crystal monitor (QCM), which is also shown in the Fig. 1. The QCM was mounted on an arm that rotated about the same axis as the one used for target rotation. The QCM sensor was swept on an arc that was 17.8 cm in radius and was oriented so its sensing face remained pointed at the midpoint of the ion beam impact zone as suggested in Fig. 1. Mass accumulation rates were typically measured over the atom ejection angle (α) range from α=-90° to α=+90° relative to the target surface normal vector in 10° to 15° increments. The polar angle range from 0 to +90 is referred to as the front half of the hemisphere located above the target, and the range from –90 to 0 is referred to as the back half. Material sputtered in the forward direction is detected in the front half of the hemisphere and material sputtered backward (toward the incident ion beam for example) is detected in the back half of the hemisphere. In is noted that QCM measurements were not made at positions where the monitor would intercept the ion beam and where structural interference between the QCM monitor and vacuum chamber structure occurred. In addition, the quartz crystal in the monitor was replaced each time a new material was tested to ensure adequate bandwidth of the QCM was available for the next test.

QCM data were obtained as changes in mass on the QCM crystal over prescribed intervals of time (several minutes) at each QCM position. Data collection was repeated as necessary to assure the mass accumulation rate had reached a stable value before final measurements were recorded. During data collection, the total and partial pressures within the vacuum facility were monitored in nitrogen equivalent units using a residual gas analyzer (RGA). The total pressure was typically in the low 10^{-5} Torr range and xenon was the dominant gas in the chamber at a nitrogen equivalent partial pressure that was very close to the total pressure. Nitrogen (and/or carbon monoxide) was the dominant impurity present during data collection at a partial pressure that was a few percent of the total pressure. Other impurities that were present during data collection were at an order of magnitude lower partial pressure and included oxygen, water

vapor, and helium. When the ion beam source was turned on and ions began to strike a given target material, the 28-amu partial pressure signal would typically rise and then decay slowly over a period of hours, thereby suggesting that either nitrogen was being released from warming surfaces or CO was being produced from the hot filament used in the discharge chamber of the ion source. Oxygen and water vapor partial pressures would generally drop slightly when the beam was first turned on. No other impurities that could be detected by the RGA (<300 amu) were observed.

One important concern during sputter yield measurements is the need for dynamically clean target surfaces.[9] This is because the presence of background gases adsorbed onto the target surface can mask the true sputter yield behavior of the material. A particularly troublesome background gas that is known to affect sputter yields of metal targets is nitrogen. One can estimate the fraction of the target covered with background gases using the following equation

$$\eta_n = \frac{\beta_n \, \dot{n}_n}{Y_n \, \dot{n}_i} \leq 0.1 \quad . \tag{1}$$

In Eq. (1), β_n represents the sticking coefficient of a neutral gas atom (n), $\dot{n}_n$ the rate of arrival of neutral particles to the target surface, Y_n the sputter yield of an adsorbed atom, and $\dot{n}_i$ the rate of arrival of bombarding ions. As a general rule of thumb, a value of η_n less than 0.1 will ensure that background gases will not affect sputter yield measurements significantly, and, during our experiments, worst case estimates of the background gas shielding effect (η_n) calculated using Eq. (1) were less than 0.05.

Measurements made at various polar angles (α) using the QCM provide mass accumulation rates [$R(\alpha)$] in gm/sec. These can be converted into units of atoms/sec by dividing the mass rates by the molecular mass of the sputtered material (M in gm/mol) and multiplying by Avagadro's number (N_A in atoms/mol). These results are converted into fractional sputter yields by dividing by the ion arrival rate, i.e. by the ion current (J) in coul/sec over the ion charge (q) in coul/ion. However, these yields represent only those atoms sputtered onto the QCM sensor through the solid angle subtended by the sensor from the region of beam impact. Because the sensor is swept through a circular arc and its surface always remains normal to the radius vector this solid angle is the same for each measurement. Assuming the ion impact region is small compared to the arc radius, the solid angle is equal to the sensor area (A_s) divided by the square of the arc radius (r). Dividing the fractional sputter yields by the solid angle subtended by the sensor gives angle-dependent differential sputter yields [$y(\alpha)$]. The equation for differential sputter yield in atoms/ion/steradian developed as it has been described above is:

$$y(\alpha) = \frac{R(\alpha) \, N_A \, q \, r^2}{M \, J \, A_s} \, . \tag{2}$$

Typical data obtained for 1 keV xenon ions sputtering titanium at a beam current of 15 mA are shown in Fig. 2. The constants needed in Eq. (1) to convert raw rate data [$R(\alpha)$] into differential yield data for this figure are:

$N_A = 6.023\text{x}10^{23}$ atoms/mol	$q = 1.6\text{x}10^{-19}$ coul/ion	$r = 17.8$ cm
$M = 47.9$ gm/mol (titanium)	$J = 15\ \text{x}10^{-3}$ coul/sec	$A_s = 0.535\ \text{cm}^2$.

It should be possible to obtain the total sputter yield by integrating a function describing the variation in differential yield with α over the full solid angle range through which atoms can be sputtered (2π steradians). For the case of normal incidence, where an axi-symmetric distribution is assumed to exist, the differential solid angle is given by

$$d\psi = \frac{2\pi \, r \sin(\alpha) \, r \, d\alpha}{r^2} = 2\pi \sin(\alpha) \, d\alpha \quad . \tag{3}$$

The total yield is then given by

$$Y = \int_0^{\frac{\pi}{2}} 2\pi \sin(\alpha) \, y(\alpha) \, d\alpha = \int_{-\frac{\pi}{2}}^{\frac{\pi}{2}} \pi \sin(\alpha) \, y(\alpha) \, d\alpha \quad . \tag{4}$$

Fig. 2a   Differential sputter yield measurements for Xe ions on a Ti target (normal incidence).

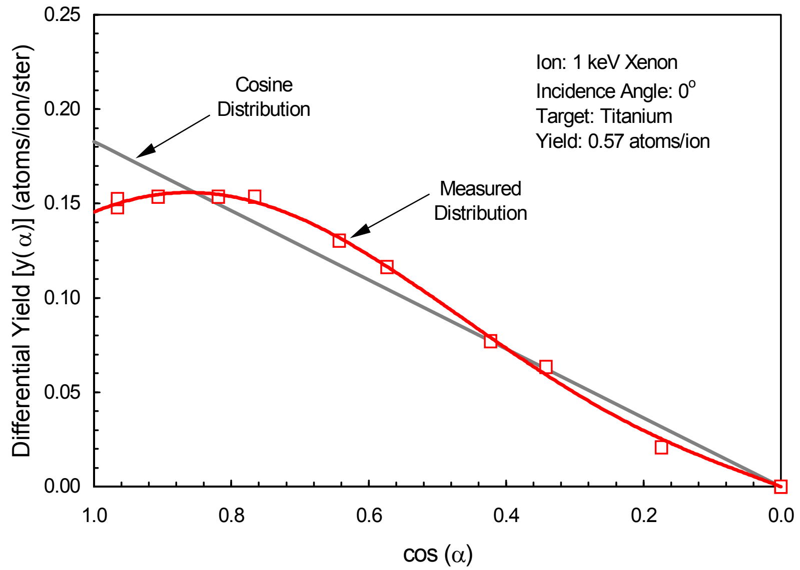

Fig. 2b   Differential sputter yield measurements for Xe ions on a Ti target (30° incidence).

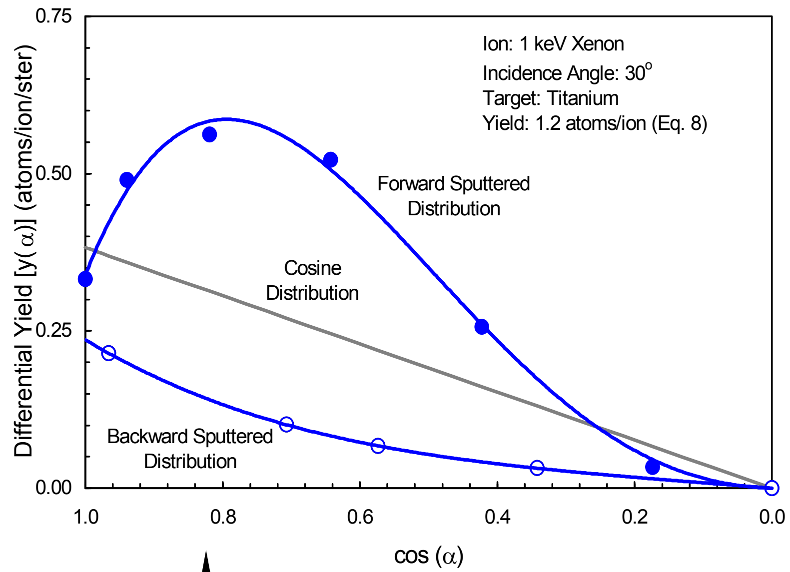

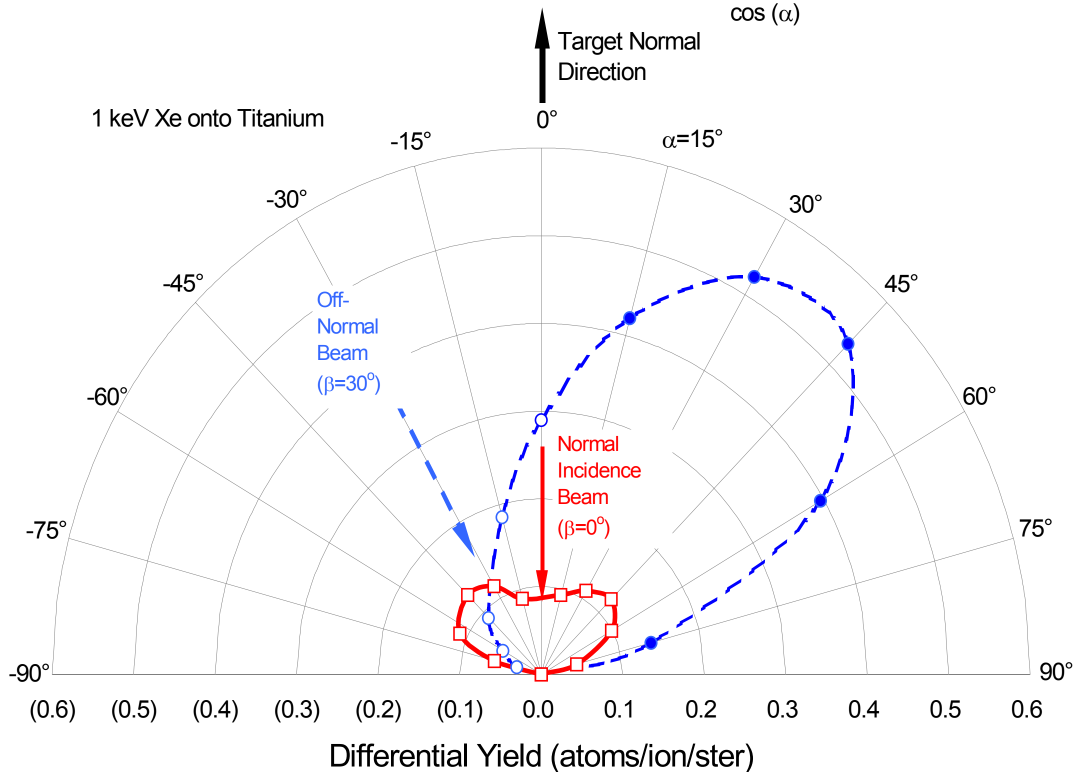

Fig. 2c   Polar plot of differential sputter yield measurements for Xe ions on a Ti Target (0° and 30° incidence).

For the normal incidence data in this report, the total yield was determined by fitting the differential yield data like those for normal incidence in Fig. 2a using up to a sixth-order polynomial and performing the integration analytically.[10]

In order to obtain total yield data for non-normal incidence data, it would be necessary to measure differential yields over the entire hemisphere above the target [i.e. obtain $y(\alpha, \phi)$ where ϕ is the azimuthal angle] and then integrate the equation:

$$Y = \int_0^{2\pi} \int_0^{\frac{\pi}{2}} 2\,\pi \sin(\alpha)\, y(\alpha, \phi)\, d\alpha\, d\phi \quad . \tag{5}$$

However, approximate values of the total yields can be obtained for non-normal incidence yield profiles (like the one for 30° shown in Fig. 2b) using the far RHS form of Eq. 4 and expressions for each half of the hemisphere located above the target surface. This approximation assumes that the variation in the azimuthal direction varies smoothly between values measured in the plane formed by the target normal and the ion beam. If the differential sputter yield data are curve-fit using Eqs. (6) and (7) for the front and back halves of the hemisphere located above the target., respectively, the total yield can be found analytically using Eq. (8).

$$y(\alpha) = A_6 \cos^6(\alpha) + A_5 \cos^5(\alpha) + A_4 \cos^4(\alpha) + A_3 \cos^3(\alpha) + A_2 \cos^2(\alpha) + A_1 \cos(\alpha) \tag{6}$$

$$y(\alpha) = B_6 \cos^6(\alpha) + B_5 \cos^5(\alpha) + B_4 \cos^4(\alpha) + B_3 \cos^3(\alpha) + B_2 \cos^2(\alpha) + B_1 \cos(\alpha) \tag{7}$$

$$Y = \frac{\pi}{n+1} \sum_{n=1}^{6} A_n + \frac{\pi}{n+1} \sum_{n=1}^{6} B_n \tag{8}$$

The polar plot of the differential sputter yield data for normal (0º) and 30º incident xenon ions shown in Fig. 2c reveals dramatic differences between the two data sets more readily than those shown in Figs. 2a and 2b. The lighter gray lines shown in Fig. 2a and 2b that are labeled "Cosine Distribution" correspond to perfectly diffuse emission of atoms from the Ti target normalized to the total yield values listed in the figure legends. The cosine distributions were calculated using values of total yield found from Eq. (8) and the diffuse emission equation presented by Mahan:[11]

$$y(\alpha) = \frac{Y \cos(\alpha)}{\pi} \quad . \tag{9}$$

Differential sputter yield data that lie below the cosine distribution at small polar angles and above at high polar angles are said to display under-cosine behavior (see Fig. 2a for example). The opposite condition of high differential sputter yields at small polar angles is referred to as over-cosine behavior (see the forward distribution shown in Fig. 2b for example). These same conditions are shown in Fig. 2c as a flattened circular shape for the 1 keV, normal incidence ion beam (under-cosine) and a forward-extended cigar shape for the 30° incident ion beam (over-cosine). It is noted that an over-cosine distribution can also be generated from normal-incidence ion beams when higher ion energies are used. The results section of this paper contains more detail on sputtering of titanium and also presents data obtained to date on molybdenum, Poco graphite, and flexible graphite (grafoil).

EXPERIMENTAL RESULTS

In addition to the 1 keV data presented in Fig. 2, we have measured differential sputter yields of Ti at xenon ion energies of 0.75, 5, and 10 keV, and Fig. 3 contains plots of these data measured at normal incidence. Figure 4 contains similar plots, but at an ion incidence angle of 30°. Several conclusions can be drawn from the data collected to date on Ti including (1) normal incident xenon ions at 1 keV and less sputter Ti into an under-cosine distribution, (2) higher ion energies of 5 and 10 keV at normal incidence cause over-cosine sputtering behavior, (3) significant forward sputtering occurs under oblique ion bombardment at low ion energies (0.75 and 1 keV), but higher ion energies (~10 keV) result in more cosine-like behavior.

Table 1 contains a list of the total yield calculated from curve fits to data like those shown in Figs. 2, 3, and 4. The front (A_n) and back (B_n) coefficients are also provided in Table 1, and they can be used in Eqs. (6) and (7) to calculate differential sputter yield distributions in the front and back halves of the hemisphere above the target (see Fig. 1). It is noted that all normal incidence data have been assumed to be symmetric and were fit in a way that forced the A_n and B_n coefficients to be equal to one another. A comparison to data

Fig. 3a Differential sputter yield measurements for 750 eV Xe ions on a Ti target (normal incidence)

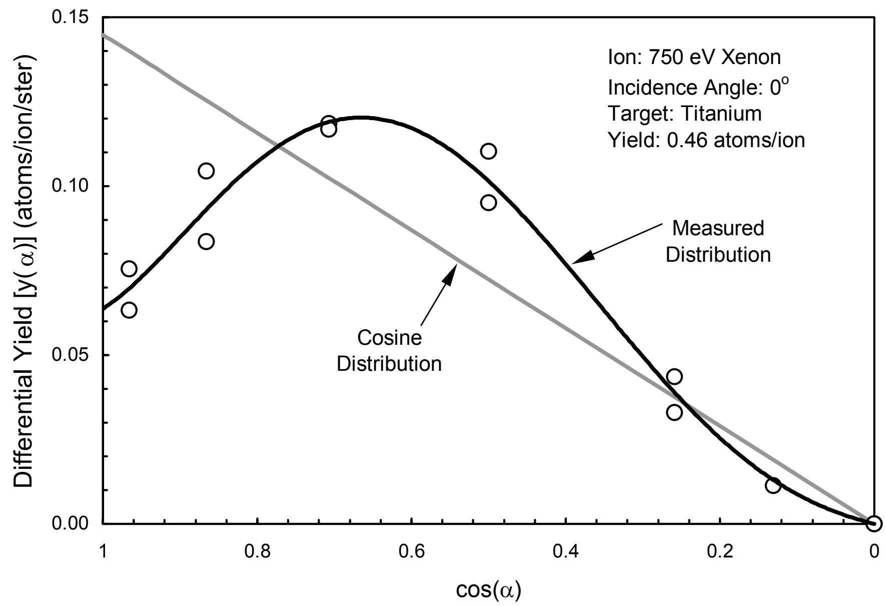

Fig. 3b Differential sputter yield measurements for 5 keV Xe ions on a Ti target (normal incidence)

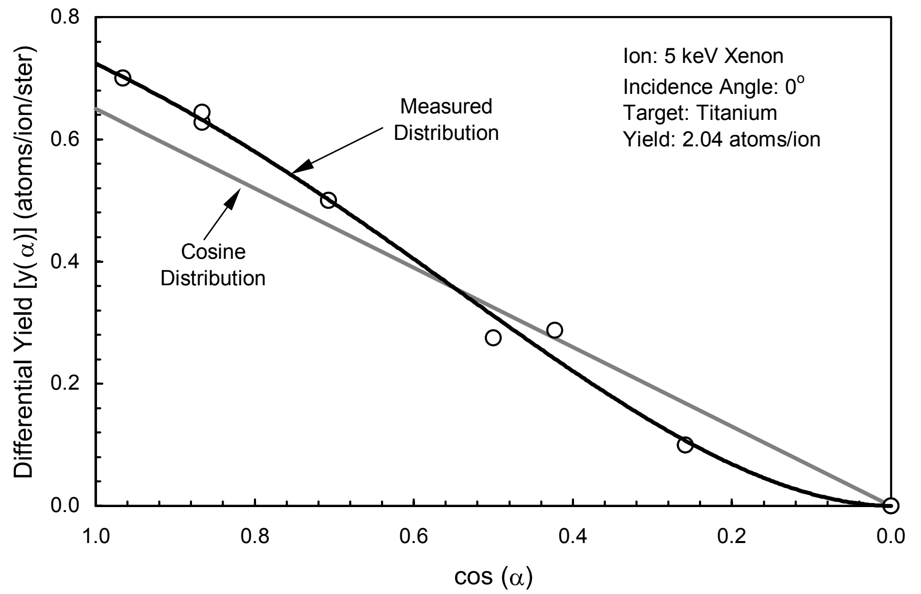

Fig. 3c Differential sputter yield measurements for 10 keV Xe ions on a Ti target (normal incidence)

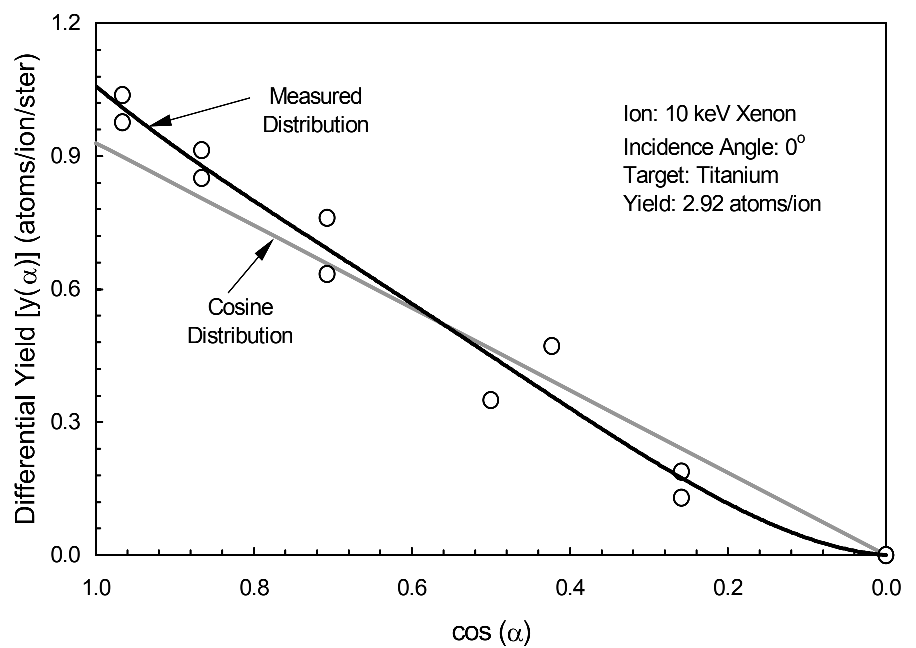

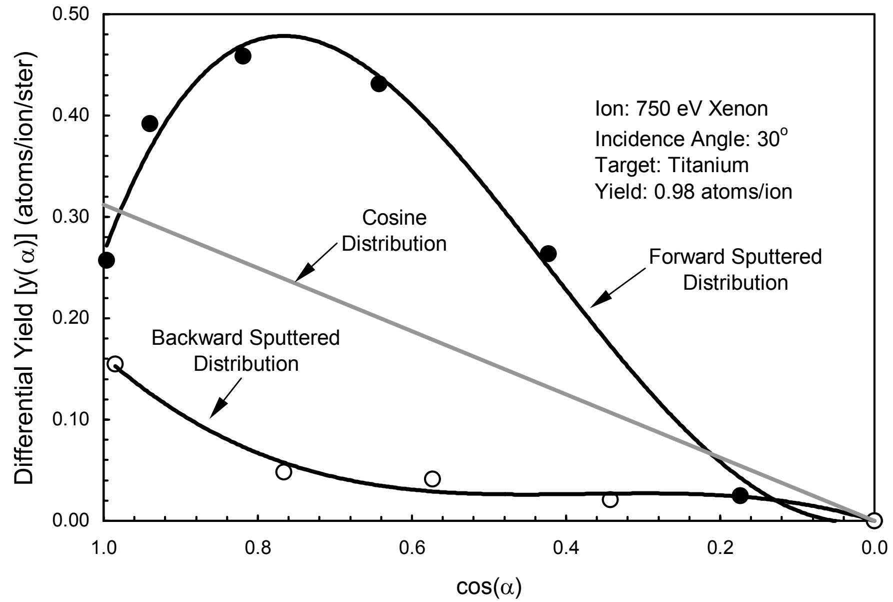

Fig. 4a Differential sputter yield measurements for 750 eV Xe ions on a Ti target (30° incidence)

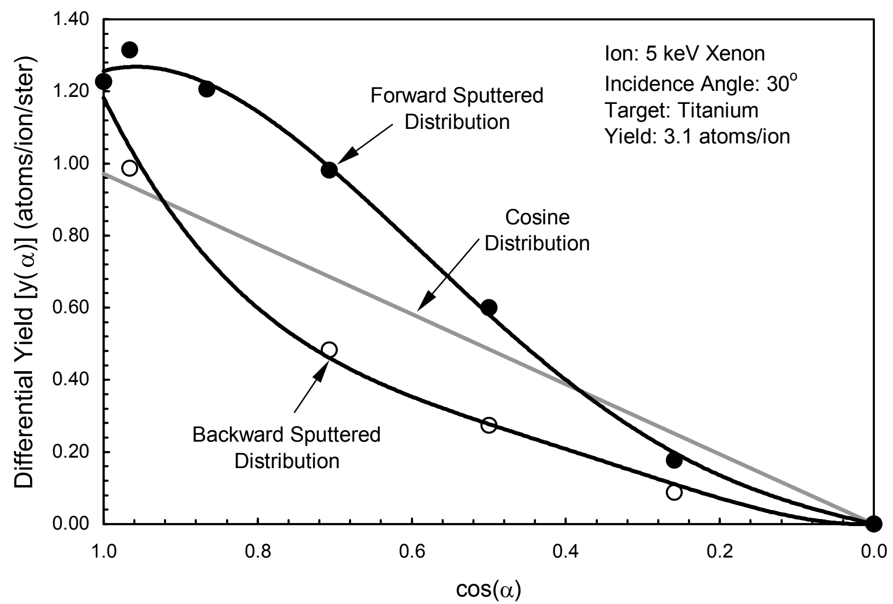

Fig. 4b Differential sputter yield measurements for 5 keV Xe ions on a Ti target (30° incidence)

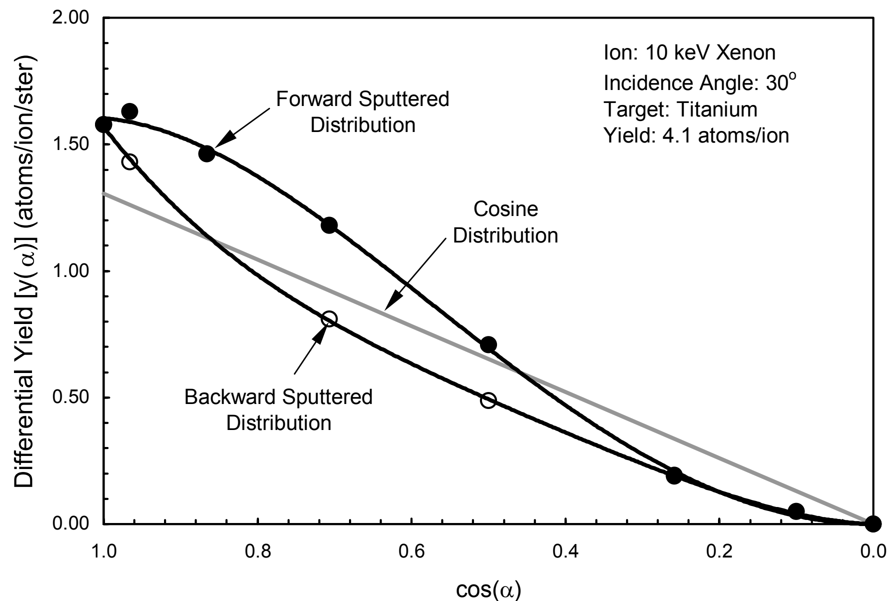

Fig. 4c Differential sputter yield measurements for 10 keV Xe ions on a Ti target (30° incidence)

TABLE 1. Sputter yield data with curve fit coefficients for material sputtered in the front and back half of the hemisphere above the target.

Xe Ion Energy (keV)	Incident Angle (degrees)	Target	Eq. (8) Total Yield (Atoms/Ion)	Front Coefficients (Atoms/Ion/Ster) [See Eq. (6)]						Back Coefficients (Atoms/Ion/Ster) [See Eq. (7)]					
				A_6	A_5	A_4	A_3	A_2	A_1	B_6	B_5	B_4	B_3	B_2	B_1
0.75	70	Ti	1.28	0.00	0.00	-2.5307	4.2455	-1.3406	0.30481	0.00	0.00	0.00	0.85294	-0.67851	0.32108
0.75	30	Ti	0.98	0.00	0.00	-0.77935	-1.1320	2.2905	-0.11526	0.00	0.00	0.00	0.58164	-0.65332	0.23418
0.75	0	Ti	0.46	0.00	1.4989	-3.0463	1.3823	0.16858	0.060237	0.00	1.4989	-3.0463	1.3823	0.16858	0.06024
1	30	Ti	1.21	0.00	0.00	-2.6180	1.8771	1.0431	0.037275	0.00	0.00	0.109248	0.05217	-0.01147	0.08599
1	15	Ti	0.67	0.00	-0.19684	0.30331	-1.0676	0.96899	0.13023	0.00	0.35928	0.071260	-0.85573	0.45104	0.10465
1	0	Ti	0.57	0.085289	0.25468	-1.1560	0.90689	-0.083432	0.13811	0.085289	0.25468	-1.1560	0.90689	-0.083432	0.13811
5	30	Ti	3.05	0.00	0.50953	-4.1325	4.1675	0.21211	0.50018	0.00	0.00	3.8064	-5.7174	3.1696	-0.076229
5	15	Ti	2.24	0.00	-3.0292	4.1140	-1.5556	1.0170	0.29435	0.00	0.00	1.9556	-3.2911	2.1019	0.058566
5	0	Ti	2.04	0.00	0.00	0.38101	-1.5660	1.8845	0.02437	0.00	0.00	0.38101	-1.56602	1.88448	0.02437
10	30	Ti	4.10	0.00	0.00	-1.2147	-0.53310	3.3577	-0.006299	0.00	0.00	2.9601	-5.0330	3.5357	0.10641
10	15	Ti	3.10	0.00	2.0380	-6.2324	5.2411	-0.38913	0.51944	0.00	0.00	1.3825	-2.5315	2.0597	0.24664
10	0	Ti	2.92	0.00	0.00	1.4194	-3.3361	2.8380	0.13677	0.00	0.00	1.4194	-3.3361	2.8380	0.13677
1	70	Mo	1.88	0.00	0.00	0.00	0.00	0.54606	0.18312	0.00	0.00	0.00	0.77987	-0.70438	0.72835
1	30	Mo	1.47	0.00	14.694	-32.016	21.029	-3.7610	0.58391	11.914	-20.874	10.331	-1.1839	0.17035	0.15517
1	15	Mo	1.03	0.00	7.9337	-17.148	10.825	-1.4714	0.17211	0.00	9.3974	-20.038	14.003	-3.6349	0.57342
1	0	Mo	0.95	0.00	5.6054	-11.417	6.4273	-0.54326	0.14880	0.00	5.6054	-11.417	6.4273	-0.54326	0.14880
5	70	Mo	5.64	0.00	0.00	0.00	4.4926	-3.5455	1.5714	0.00	0.00	9.4331	-14.898	7.2210	0.99778
5	30	Mo	3.99	0.00	47.995	-103.52	72.219	-16.035	1.3682	0.00	25.386	-45.114	24.269	-3.2599	0.78801
5	15	Mo	3.09	0.00	27.551	-57.785	38.020	-6.7903	0.49263	0.00	18.175	-31.821	15.803	-1.0248	0.37464
5	0	Mo	2.40	4.8460	0.46257	-13.813	10.244	-1.0098	0.30257	4.8460	0.46257	-13.813	10.244	-1.0098	0.30257
10	70	Mo	6.76	0.00	0.00	0.00	2.7497	-1.8869	1.4204	0.00	-13.055	38.469	-41.913	18.652	0.25070
10	30	Mo	4.94	0.00	12.034	-19.980	6.4773	3.3374	0.37923	0.00	21.885	-37.893	18.370	-0.38789	0.21854
10	15	Mo	4.45	0.00	-3.7836	15.679	-20.195	9.8999	0.32601	0.00	9.2718	-15.258	5.5562	1.8794	-0.02605
10	0	Mo	3.90	0.00	-1.8631	9.4615	-13.396	7.2141	-0.03303	0.00	-1.8631	9.4615	-13.396	7.2141	-0.03303
0.75	70	Poco	0.60	0.00	-3.6637	7.6836	-5.6217	1.7152	0.08079	0.00	0.00	1.17032	-1.9046	0.93493	-0.02224
0.75	30	Poco	0.40	0.00	0.00	0.099762	-1.0975	0.99170	0.06546	0.00	0.00	0.00	-0.03084	0.06537	0.01035
0.75	0	Poco	0.29	0.00	0.00	0.00	0.17543	-0.40546	0.27443	0.00	0.00	0.00	0.17543	-0.40546	0.27443
1	30	Grafoil	0.46	0.00	0.031529	0.29908	-0.98141	0.54387	0.19820	0.00	0.00	-0.12960	0.32517	-0.26152	0.15467
1	15	Grafoil	0.41	0.00	0.00	0.63566	-1.2848	0.44053	0.26976	0.00	0.00	0.00	0.46132	-0.73850	0.34628
1	0	Grafoil	0.39	0.00	-1.4588	3.5666	-2.8471	0.52865	0.25361	0.00	-1.4588	3.5666	-2.8471	0.52865	0.25361
5	30	Grafoil	1.56	0.00	-0.50665	1.2244	-2.4823	1.9093	0.26282	0.00	0.00	1.9469	-3.2422	1.4152	0.27716
5	15	Grafoil	1.51	0.00	0.00	-0.43215	-0.14879	0.41578	0.54766	0.00	0.00	1.0292	-1.5307	0.40559	0.46450
5	0	Grafoil	1.55	0.00	0.00	1.5114	-2.8507	1.2420	0.48715	0.00	0.00	1.5114	-2.8507	1.2420	0.48715
10	30	Grafoil	2.86	0.00	0.00	1.8312	-5.3562	3.9228	0.29043	0.00	0.00	-9.1156	16.168	-8.3078	1.9604
10	15	Grafoil	2.47	0.00	0.00	3.0716	-6.1462	3.1665	0.59867	0.00	0.00	2.2021	-3.4675	1.3220	0.67705
10	0	Grafoil	2.26	0.00	4.2781	-4.7859	-0.43686	0.86866	0.84811	0.00	4.2781	-4.7859	-0.43686	0.86866	0.84811

collected by Rosenberg and Wehner[12] and a curve-fit suggested by Yamamura and Tawara[13] is shown in Fig. 5a. The data we collected falls ~20% below the curve in Fig. 5a at low ion energy (0.75 and 1 keV) and ~20% above the curve at high energies (5 and 10 keV). In addition to data on Ti, Table 1 also contains data collected to date on molybdenum, Poco graphite, and flexible graphite (grafoil). Figure 5b shows comparisons between our data on Mo at normal incidence and values obtained by Rosenberg and Wehner.[12] Our data were observed to fall slightly below the curve fit suggested by Yamamura and Tawara,[13] which was derived from data collected by several different researchers in addition to Rosenberg and Wehner.

Differential sputter yield data are presented in Fig. 6 for xenon ion sputtering of molybdenum. The sample chosen for this test was a ~15cm x 22 cm x 0.51 mm, arc-cast, cross-rolled molybdenum sheet that is typically used to fabricate grids for ion thrusters. The sample was tested in an as-received condition after light cleaning with a commercial de-greasing formula and water rinse. Figure 6a shows polar plots of data collected at 1 keV of ion energy including the corresponding data point on Fig. 5b. The normal incidence data were observed to be non-symmetric with more material being sputtered into the left half of the hemisphere above the target. The sputtered distribution from the 30° incident ion beam was observed to forward sputter Mo, but in a two-lobe manner. Finally, the 70° incident ion beam was observed to generate a nearly symmetric cosine sputtered distribution, with a slight over-cosine characteristic in the back hemisphere direction and a slight bulge in the front hemisphere direction.

Figure 6b contains polar plots corresponding to 0°, 30°, and 70° incident ions at 5 keV. The normal incidence data (along with the 30° and 70° data) were observed to be much more symmetric than the 1 keV distributions, and all of the sputtered distributions at 5 keV are observed to be over-cosine in shape. Similar results were observed for sputtering by 10 keV ions as shown in Fig. 6c, except for the 70° data, which show high cosine-like, back-sputtered concentrations.

A limited amount of data were taken using an electronic-grade graphite plate (Poco Graphite AFX-5Q) as the sputter target, and a polar plot of the data collected at a xenon ion energy of 750 eV is shown in Fig. 7a for angles of incidence of 0°, 30°, and 70°. For this sample, the normal incident beam was observed to sputter material in a highly under-cosine manner. As indicated in Table 1, the sputter yield for normal incidence was calculated to be 0.29 atoms/ion, which compares well to a value of 0.27 measured by Deltschew et al.[14] using PT 2120, an electronics grade graphite plate from Carbone Lorraine. Data for 30° incident ions show a substantial forward sputtered character, while the data for 70° incident ions display a less forward and more symmetric over-cosine distribution. Figure 7b contains polar plots of sputtered grafoil (flexible graphite sheet) that were measured at 1 keV of ion energy at incident angles of 0°, 15°, and 30°. In contrast to the graphite sheet data, all the grafoil data at 1 keV were observed to be under-cosine, and, in addition, calculated values of sputter yield shown in Table 1 varied very little with incident angle. Similar trends were observed for grafoil at an ion energy of 5 keV where the sputtered yield remained nearly constant as the incident angle was varied from 0° to 30°. The largest incident angle-induced variation in sputter yield for grafoil was observed at 10 keV. It is also noted that the normal incidence sputter yield for grafoil is not much less than Ti at 10 keV. In addition, considering possible contamination from binders used in the fabrication of grafoil, this material would not be a good choice for the beam dump in a test facility designed to evaluate high specific impulse ion thrusters.

CONCLUSIONS AND RECOMMENDATIONS FOR FUTURE WORK

Xenon ion sputtering yields were measured over an energy range from 750 eV to 10 keV and an angle of incidence range of 0 to 70 for several materials used in ion thruster devices and test facilities. The sputtering yield measurement technique utilized a quartz crystal monitor that was swept at constant radial distance from a small target region where a high current density xenon ion beam was aimed. This technique appears to provide sputter yield data that are in good agreement with the available literature. A particularly useful feature of this technique is the ability to obtain differential sputter yield data quickly at relatively low cost using modest test facilities. It is argued that these data would be valuable to analysts who are attempting to model the wear profile of an ion optics system throughout a given mission. Recommendations for future work include (1) extending the measurements to lower ion energies and higher angles of incidence and (2) documenting the differential sputter yield over the entire hemisphere above the target. Other important future work will be to measure the sputtering behavior of advanced carbon-carbon composite materials that are being considered for ion optics systems in the near future. Finally, we believe that evaluation of existing

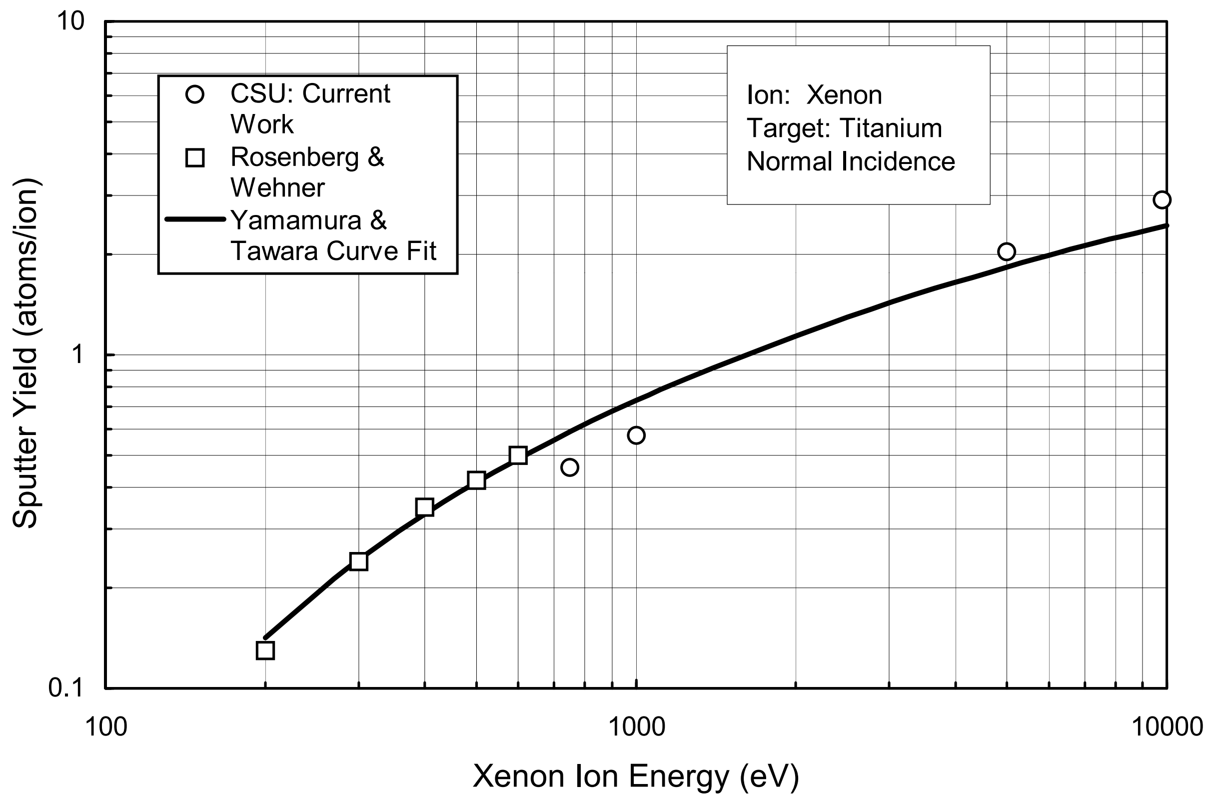

Fig. 5a Comparison of Ti sputter yield data to Rosenberg and Wehner

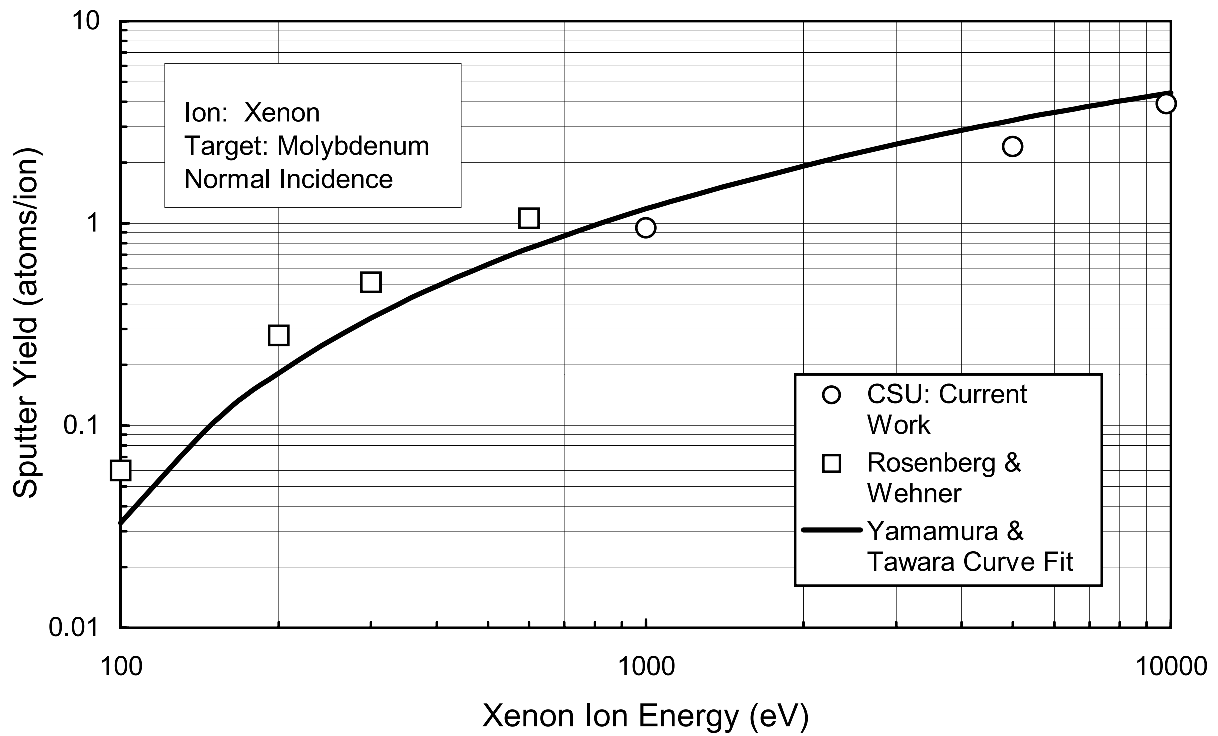

Fig. 5b Comparison of Mo sputter yield data to Rosenberg and Wehner

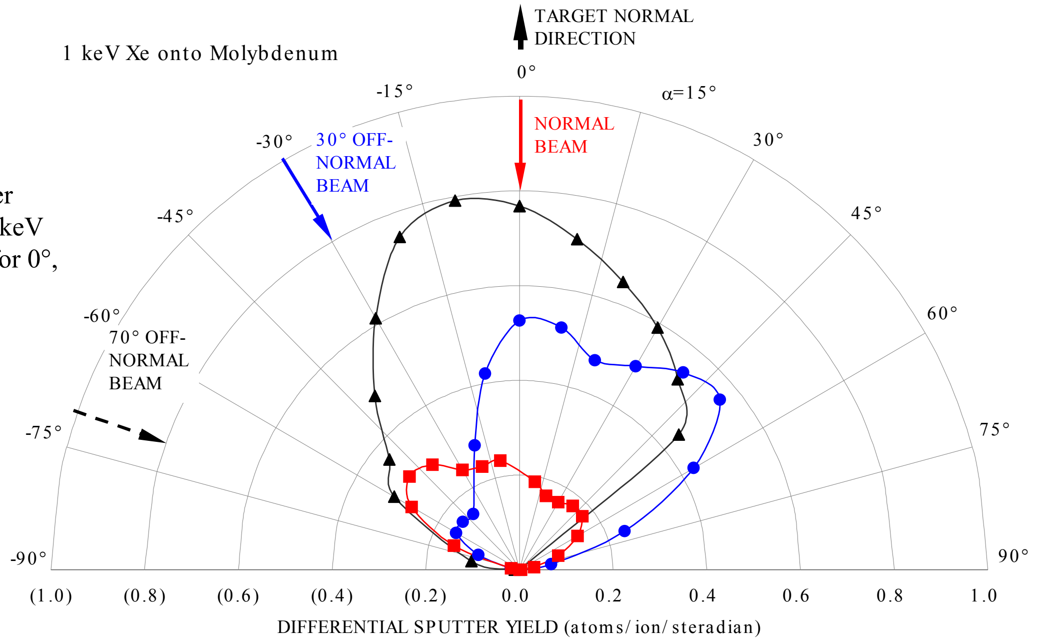

Fig. 6a Differential sputter yield measurements for 1 keV Xe ions on a Mo target (for 0°, 30°, and 70° incidence)

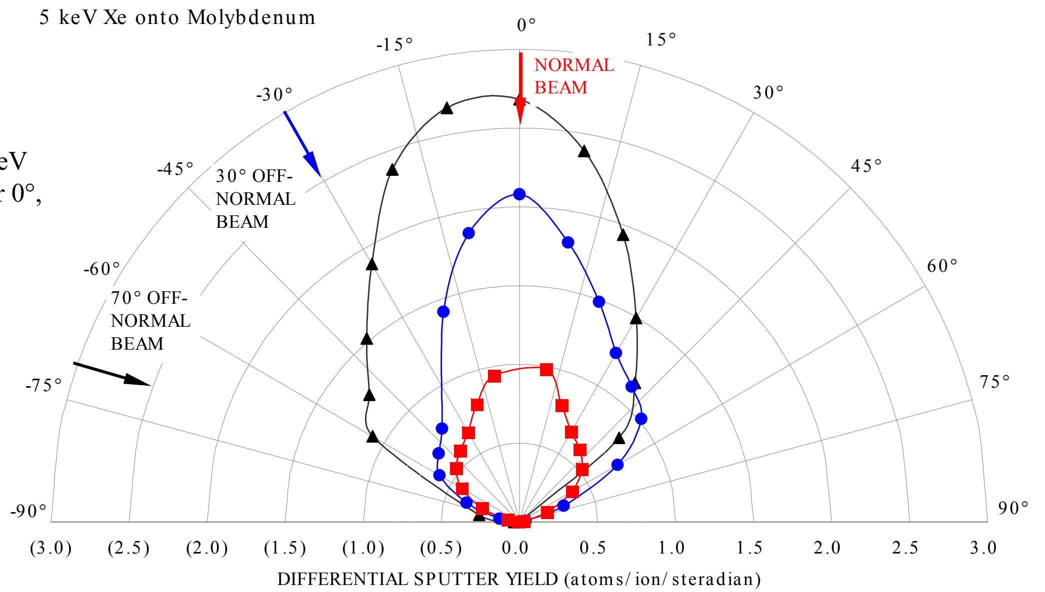

Fig. 6b Differential sputter yield measurements for 5 keV Xe ions on a Mo target (for 0°, 30°, and 70° incidence)

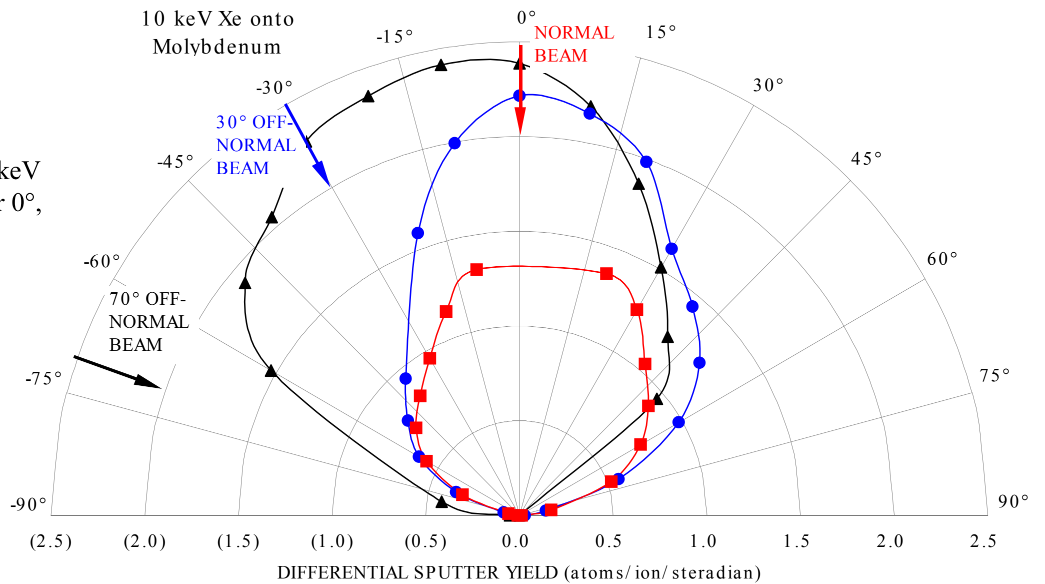

Fig. 6c Differential sputter yield measurements for 10 keV Xe ions on a Mo target (for 0°, 30°, and 70° incidence)

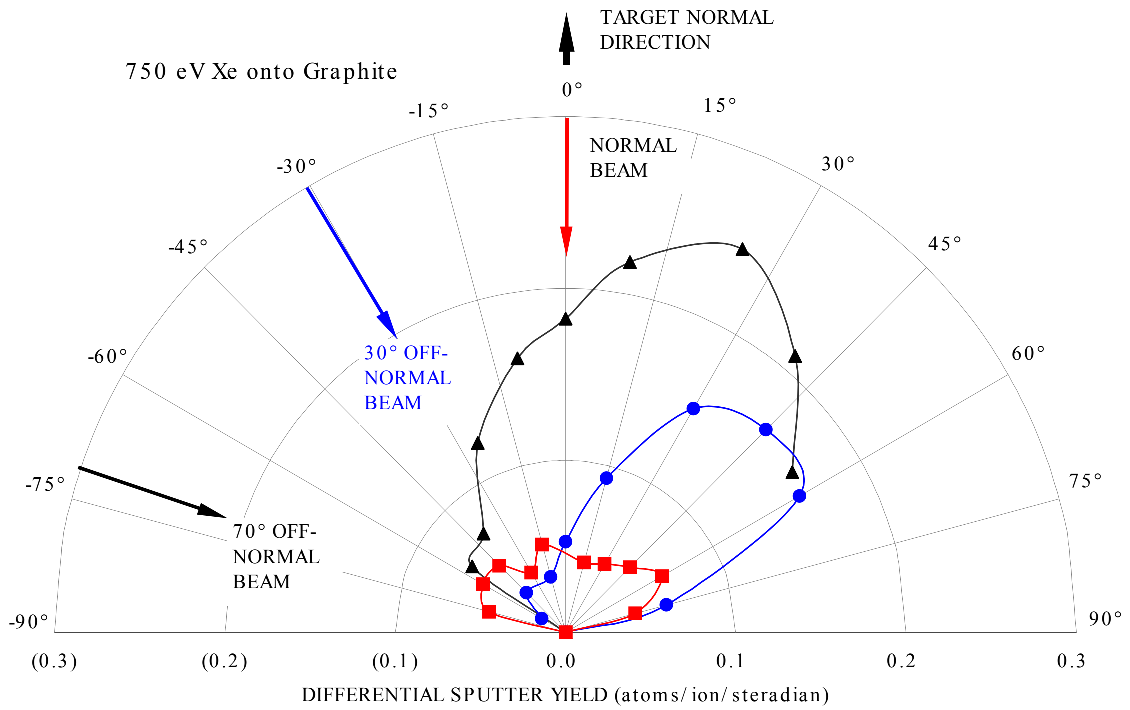

Fig. 7a Differential sputter yield measurements for 750 eV Xe ions on a Poco graphite target (for 0°, 15°, and 30° incidence)

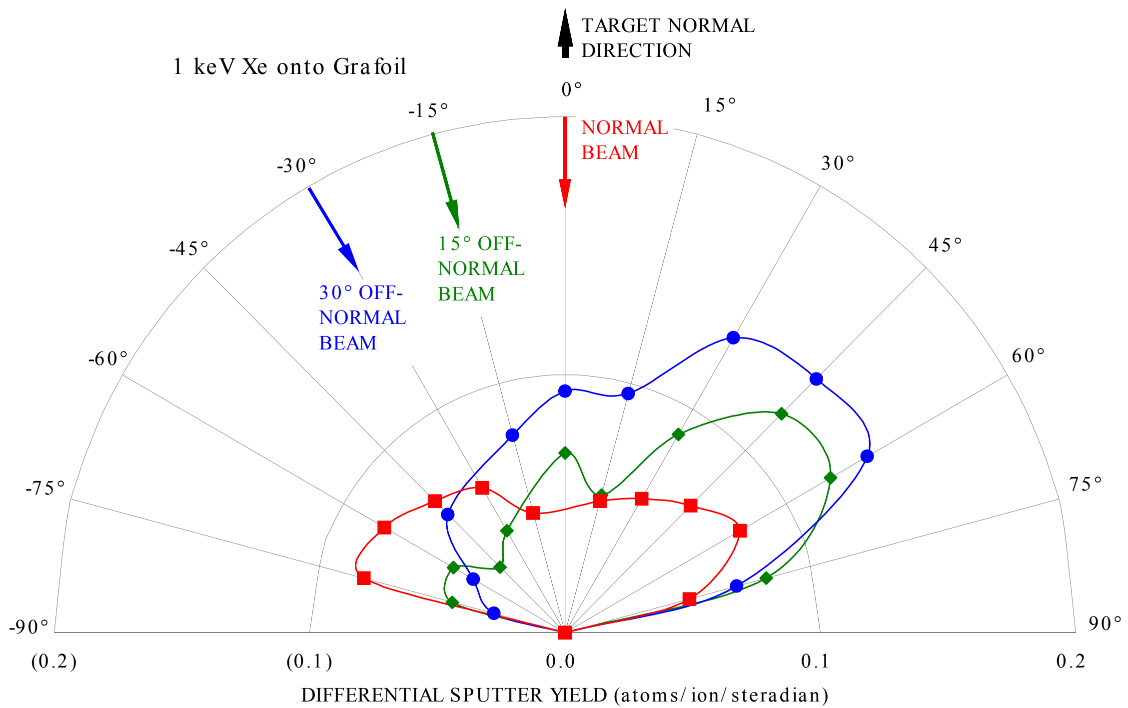

Fig. 7b Differential sputter yield measurements for 1 keV Xe ions on a flexible graphite (grafoil) target (for 0°, 15°, and 30° incidence)

(and development of new) analytical and numerical sputtering models that give differential sputter yields should be pursued in parallel with an experimental effort in an attempt to "fill in the gaps" that would occur in an experiment-only program.

ACKNOWLEDGMENTS

Partial financial support under Research Grant NAG3-1801 through the NASA Glenn Research Center is gratefully acknowledged for P.J. Wilbur and M.M. Gardner.

REFERENCES

[1] C.C. Farnell, J.D. Williams, and P.J. Wilbur, "Numerical Simulation of Ion Thruster Optics," 28th International Electric Propulsion Conference, IEPC-03-073, Toulouse, France, 17-21 March 2003.

[2] Y. Nakayama and P.J. Wilbur, "Numerical Simulation of High Specific Impulse Ion Thruster Optics," 27th International Electric Propulsion Conference, IEPC-01-099, Pasadena, CA, 2001.

[3] J.D. Williams, D.M. Laufer, and P.J. Wilbur, "Experimental Performance Limits on High Specific Impulse Ion Optics," 28th International Electric Propulsion Conference, IEPC-03-128, Toulouse, France, 17-21 March 2003..

[4] P.J. Wilbur, J. Miller, C.C. Farnell, and V.K. Rawlin, "A Study of High Specific Impulse Ion Thruster Optics," 27th International Electric Propulsion Conference, IEPC-01-098, Pasadena, CA, 2001.

[5] C.C. Farnell, J.D. Williams, and P.J. Wilbur, "Characteristics of Energetic Ions Emitted from Hollow Cathodes," 28th International Electric Propulsion Conference, IEPC-03-072, Toulouse, France, 17-21 March 2003.

[6] Foster, J.E. and M.J. Patterson, "Plasma Emission Characteristics from a High Current Hollow Cathode in an Ion Thruster," 38th Joint Propulsion Conference, AIAA Paper 2002-4102, Indianapolis, IN, July 2002.

[7] M.W. Crofton and I.D. Boyd, "Plume Measurement and Modeling Results for a Xenon Hollow Cathode," 38th Joint Propulsion Conference, AIAA 2002-4103, Indianapolis, IN, 2002.

[8] M.A. Mantenieks, "Sputtering Threshold Energies of Heavy Ions," 25th International Electric Propulsion Conference, IEPC-97-187, Cleveland, OH, 1997.

[9] V. Shutthanandan, P.K. Ray, N.R. Shivaparan, R.J. Smith, S. Thevuthansan, and M.A. Mantenieks, "On the Measurement of Low Energy Sputtering Yield Using Rutherford Backscattering Spectrometry," 25th International Electric Propulsion Conference, IEPC-97-069, Cleveland, OH, 1997.

[10] M.A. Mantenieks, J.E. Foster, P.K. Ray, S.V. Shutthanandan, and T.S. Thevuthasan, "Low Energy Xenon Ion Sputtering Yield Measurements," 27th International Electric Propulsion Conference, IEPC-01-309, Pasadena, CA, 2001.

[11] J. Mahan, Physical Vapor Deposition of Thin Films, John Wiley and Sons, Inc., New York, New York, 2000.

[12] D. Rosenberg and G.K. Wehner, "Sputtering Yields for Low Energy He+, Kr+, and Xe+ Ion Bombardment," J. of Applied Physics, V. 33, No. 5, pp. 1842-1845, 1962.

[13] Y. Yamamura and H. Tawara, "Energy Dependence of Ion-Induced Sputtering Yields from Monatomic Solids at Normal Incidence," Atomic Data and Nuclear Data Tables, V. 62, No. 2, pp. 149-253, 1996.

[14] R. Deltschew, M. Tartz, V. Plicht, E. Hartmann, H. Neumann, H.J. Leiter, and J. Esch, "Sputter Characteristics of Carbon-Carbon Compound Material," 27th International Electric Propulsion Conference, IEPC-01-118, Pasadena, CA, 2001.